## 9.6 The UA1 experiment

In 1976 C. Rubbia, D. Cline and P. McIntyre (Rubbia *et al.* 1976) proposed transforming the CERN Super Proton Synchrotron (SPS) into a storage ring in which protons and antiprotons would counter-rotate and collide head-on, as we have already discussed in Section 1.10. In this way, with 270 GeV per beam, the energy needed to create the $W$ and the $Z$ could be reached. To this aim a

large number of antiprotons had to be produced, concentrated in a dense beam and collided with an intense proton beam. Let us evaluate the necessary luminosity.

We can think of the proton and the antiprotons as two groups of partons, quarks, antiquarks and gluons, travelling in parallel directions, as shown in Fig. 9.11, neglecting, in a first approximation, the transverse momentum of the partons. Let us consider the valence quarks and antiquarks respectively. They carry the largest fraction of the total momentum, about 1/6 on average, with a rather broad distribution (see Fig. 6.14). It is important to notice that the width of the $\sqrt{\hat{s}}$ distribution is much larger than the widths of the $W$ and $Z$ resonances. Therefore, the $W$ and $Z$ production cross sections grow with collision energy because the larger $\sqrt{s}$ the greater the probability of finding a quark–antiquark pair with $\sqrt{\hat{s}}$ close to resonance. In conclusion, the higher the energy the better. The initial design centre of mass energy at CERN was $\sqrt{s} = 540$ GeV, to reach 630 GeV later on.

The calculation of the proton–antiproton cross sections starts from those at the quark level and takes into account the quark distribution functions and the effects of the colour field. The evaluation made in the design phase gave the values

$$\sigma(\bar{p}p \to W \to e\nu_e) \approx 530\,\text{pb} \qquad \sigma(\bar{p}p \to Z \to ee) \approx 35\,\text{pb}. \tag{9.62}$$

To be precise, both the valence and the sea quarks contribute to the process, however at $\sqrt{s} = 540$ GeV the average momentum fraction at the $W$ and $Z$ resonances is $\langle x \rangle_W / \sqrt{s} \approx 0.15$. Therefore, the process is dominated by the valence quarks, while the sea quarks have momentum fractions that are too small. We thus know that the annihilating quark is in the proton, the antiquark in the antiproton. This information is lost at higher collision energies.

As we have mentioned in Section 1.10, the stochastic cooling technique had been developed at CERN to increase the density of particles within bunches at the collision point. Starting from this experience, an advanced accelerator physics programme was launched, under the guidance of S. Van der Meer, which made it

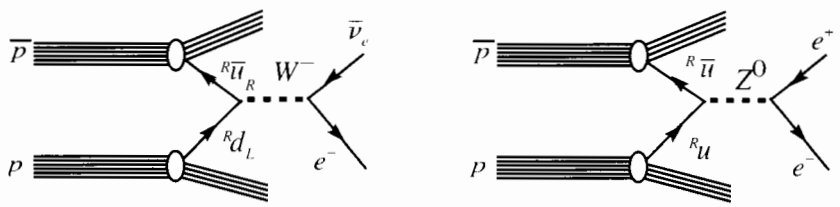


Fig. 9.11. $W$ and $Z$ production in a $\bar{p}p$ collider. Upper left indices label the colour.

possible to reach the luminosity $\mathcal{L} = 10^{32}$ m$^{-2}$ s$^{-1}$, large enough to search for $W$ and $Z$, in 1983.

*Example 9.3* How many $W \to e\nu$ events and how many $Z \to e^+e^-$ events are observed in one year with the luminosity $\mathcal{L} = 10^{32}$ m$^{-2}$ s$^{-1}$ and 50% detection efficiency? We apply the mnemonic rule that one year $= \pi \times 10^7$ s. Taking into account the time needed to fill the machine, for maintenance, etc. we take $10^7$ s. With the above-mentioned cross sections we have $\sim 25$ $W \to e\nu$ and $\sim 2$ $Z \to ee$. Actually the $W$ was discovered several months before the $Z$.

The production of weak vector bosons is a rare event. Indeed the cross sections in (9.62) are eight and nine orders of magnitude smaller than the total proton–antiproton cross section, which is 60 mb at the energies we are considering. Weak interactions are weak indeed! Consequently, the detector must be able to detect the interesting events with a discriminating power of at least $10^{10}$. This is the reason why we considered above only the leptonic channels, which can be discriminated. The hadronic channels $W \to \bar{q}q'$, $Z \to \bar{q}q$ are more frequent but are submerged in a huge background due to strong interaction processes, such as

$$gg \to gg \qquad gq \to gq \qquad g\bar{q} \to g\bar{q} \qquad q\bar{q} \to q\bar{q}. \tag{9.63}$$

The leptonic channels are

$$\bar{p}p \to W \to e\nu_e \qquad \bar{p}p \to W \to \mu\nu_\mu \qquad \bar{p}p \to W \to \tau\nu_\tau \tag{9.64}$$

and

$$\bar{p}p \to Z \to ee \qquad \bar{p}p \to Z \to \mu\mu \qquad \bar{p}p \to Z \to \tau\tau. \tag{9.65}$$

Leptons can be present in the strong interaction processes too, being produced indirectly by hadron decays, but they can be discriminated. The crucial variable is the 'transverse momentum', $p_T$, namely the momentum component perpendicular to the colliding beams. In the largest fraction of cases the proton–antiproton collision is soft, namely it gives rise to low transverse momentum hadrons. Consider one of them, for example a charm, which decays into a charged lepton. The latter might simulate one of the (9.64) or (9.65) processes. However, in the rest frame of the decaying particle the lepton momentum is a fraction of the charm mass, less than a GeV. The Lorentz transformation to the laboratory frame does not alter the lepton component normal to the charm velocity, which is about that of the beams. The transverse momenta of the kaons are even smaller, while those of the beauties are somewhat larger.

However, there are cases in which two partons come very close to each other and collide violently, namely with a large momentum transfer, by one of the

processes (9.63). These events are rare, because, as discussed in Chapter 6, the QCD coupling constant is small at high momentum transfer. The hit parton appears as a jet at high transverse momentum. A possible semileptonic decay of a hadron produces a high $p_T$ lepton. However, these leptons are inside a jet, while those from the $W$ and $Z$ decays are not. In conclusion, we search for leptons that have a high $p_T$ and are 'isolated', namely without other particles in a properly defined cone around its direction.

The same criteria also apply to the neutrino, in the case of the $W$. Even if neutrinos cannot be detected, we can infer their presence indirectly. To this aim we must build a hermetic detector, which completely surrounds the interaction point with homogeneous calorimeters, in order to intercept all the hadrons and charged leptons and to measure their energies. Moreover, the calorimeters are divided into cells, in order to measure also the direction of the particles. However, the energy of the high-energy muons cannot be measured with calorimetric means because these particles cannot be absorbed in a reasonable length. We solve the problem by determining their momenta by measuring their trajectories in a magnetic field. With this information, we check if the vector sum of all the momenta is compatible with zero or not. In the presence of one (or more) neutrinos we find an imbalance and we say that the 'missing momentum' is the momentum of the neutrino(s). This is possible even if the detector cannot be closed at small angles with the beams, where the physical elements needed to drive the beam itself are located, because we only need the *transverse* component of the missing momentum, $p_T^{miss}$, to which the undetected particles at small angles make a negligible contribution.

Summarising, the principal channels for the $W$ and $Z$ search and the corresponding topologies are

$$W \to e^{\pm}\nu_e \qquad \text{isolated electron at high } p_T \text{ and high } p_T^{miss} \tag{9.66a}$$

$$W \to \mu^{\pm}\nu_\mu \qquad \text{isolated muon at high } p_T \text{ and high } p_T^{miss} \tag{9.66b}$$

$$Z \to e^+e^- \qquad \text{two isolated electrons, opposite sign, at high } p_T \tag{9.67a}$$

$$Z \to \mu^+\mu^- \qquad \text{two isolated muons, opposite sign, at high } p_T. \tag{9.67b}$$

This discussion determines the main specifications of the experimental apparatus.

Two experiments were built at the CERN proton–antiproton collider, called UA1 and UA2. The $W$ and the $Z$ were observed by UA1 (Arnison *et al.* 1983a, 1983b) first and immediately afterwards by UA2 (Banner *et al.* 1983, Bagnaia *et al.* 1983). The results of the two experiments are in perfect agreement and of the same quality. We shall describe here those of UA1.

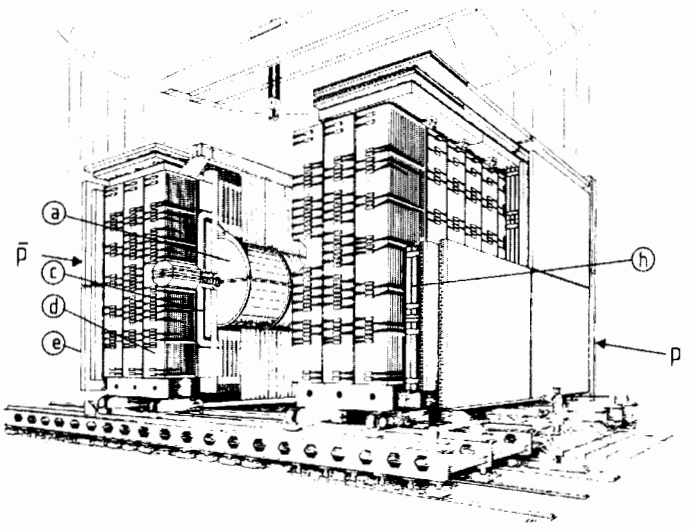


Fig. 9.12. Artist's view of the UA1 experiment, shown in its open configuration. The labels indicate the components: (a) tracking central detector, (c) magnetic field coil, (d) hadronic calorimeters, (e) drift chambers for $\mu$ detection, (h) Fe absorber. (Albajar *et al.* 1989)

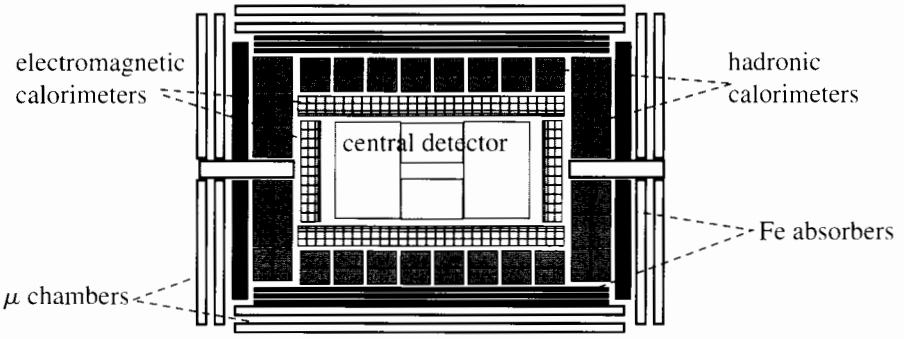


Fig. 9.13. Simplified horizontal cross section of UA1.

Figure 9.12 shows an artist's view of the UA1 experiment, when open. Figure 9.13 shows the UA1 logic structure. The two beams travelling in the vacuum pipe enter the detector from the left and the right respectively, colliding at the centre of the detector. A particle produced in the collision meets in series the following elements:

1. The central detector, which is a large cylindrical time-projection chamber providing electronic images of the charged tracks, and is immersed in a horizontal magnetic field in the plane of the drawing, perpendicular to the beams.
2. The electromagnetic calorimeters, made up of a sandwich of lead plates alternated with plastic scintillator plates. In the calorimeter electrons and photons lose all their energy, which is measured.

3. The other particles penetrate the hadronic calorimeter, which is a sandwich of iron and plastic scintillator plates. The iron plates on the left and right sides of the beams also act as the yoke of the magnet driving the magnetic return flux. In the calorimeter the hadrons lose all (or almost all) of their energy, which is measured.
4. In practice the highest-energy hadronic showers, especially in the forward directions, are not completely contained in the calorimeters, as ideally they should be. They are absorbed in iron absorbers.
5. The particles that survive after the iron absorbers are neutrinos and muons. Large tracking drift and streamer chambers detect the latter.

The detector is hermetic but at small angles with the beams; the response of the calorimeters is made as homogeneous as possible.

## 9.7 The discovery of $W$ and $Z$

Figure 9.14 shows the reconstruction of one of the first $W \to e\nu$ events observed by UA1. We observe many tracks that make the picture somewhat confused. These are particles pertaining to the 'rest of the event', i.e. coming from the interaction of partons different from those that produced the $W$. They are soft, because the strong coupling constant is large at small momentum transfers, and can be easily eliminated simply by neglecting all tracks with $p_T$ smaller than a few times $\lambda_{QCD}$, in practice with $p_T < 1$ GeV, as shown in Fig. 9.14(b).

With this simple 'cut' we are left with a clean picture of a single charged track with the characteristics of an electron. Its momentum, measured from its curvature, and its energy, measured in the calorimeter, are equal within the errors. We also find that the transverse momentum is not balanced. The transverse missing momentum is shown in Fig. 9.14(a).

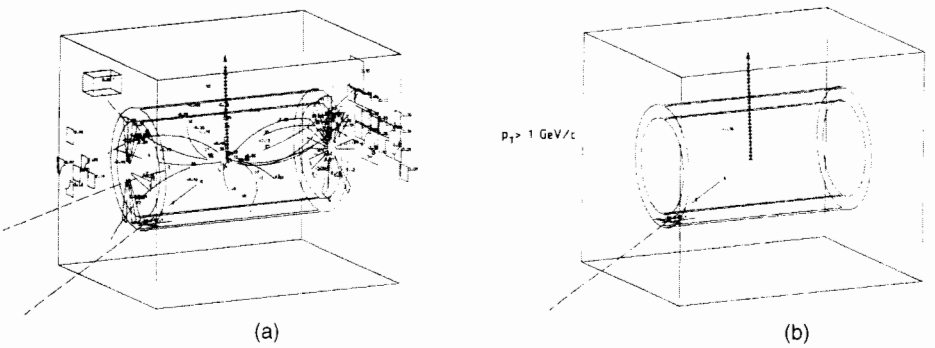


Fig. 9.14. A $W \to e\nu$ event. (a) The tracks, the hit calorimeter cells and the missing transverse momentum are shown; (b) only tracks with $p_T > 1$ GeV. (Rubbia 1985 © Nobel Foundation 1984)

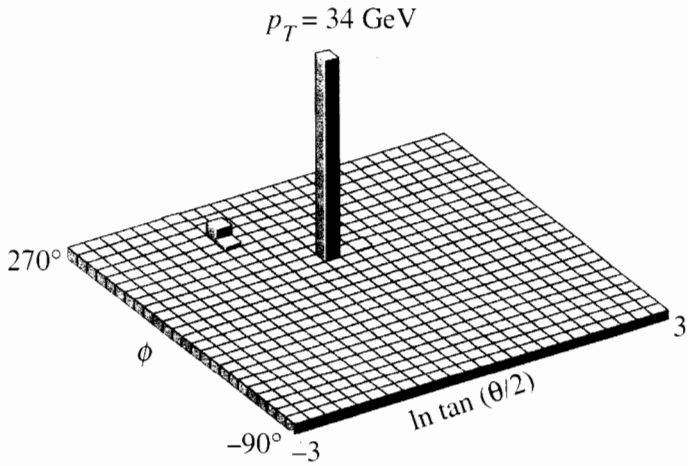


Fig. 9.15. Lego plot of a $W \rightarrow ev$ event in the electromagnetic calorimeter. $\phi$ azimuth, $\theta$ anomaly to the beam direction. (Adapted from Rubbia 1985)

The calorimeters give a complementary view of the events, namely they show the energy flow from the collision point as a function of the angles. Figure 9.15 shows such a view for a $W \rightarrow ev$ event. The cells of the diagram, called a 'lego plot', correspond to the physical electromagnetic calorimeter cells. The two coordinates are the azimuth $\phi$ and a function of the anomaly $\theta$ with the beam direction as polar axis. Since the frequency of tracks in the forward directions, namely for $\theta = 0$ and $\theta = \pi$, is very high, the function $\ln \tan \theta/2$ is used to obtain a smooth distribution. In this event there is in practice a single, large, localised energy deposit. This is how the calorimeter sees the electron.

Summarising, we see that simple kinematic selection criteria allow unambiguous identification of the very rare cases in which a $W$ is produced. It subsequently decays into $ev$.

The situation is similar for the decays into $\mu\nu$ and into $\tau\nu$, which we shall not discuss. We mention, however, that the comparison of the three cross sections gives a test of lepton universality, namely

$$\begin{aligned} g_\mu/g_e &= 1.00 \pm 0.07(\text{stat}) \pm 0.04(\text{syst}) \\ g_\tau/g_e &= 1.01 \pm 0.10(\text{stat}) \pm 0.06(\text{syst}). \end{aligned} \tag{9.68}$$

Let us now consider the measurement of the $W$ mass. As the calorimetric measurement of the electron energy is more precise than the muon momentum measurement, we choose the $ev$ channel. We cannot reconstruct the electron-neutrino mass because only the transverse component of the neutrino

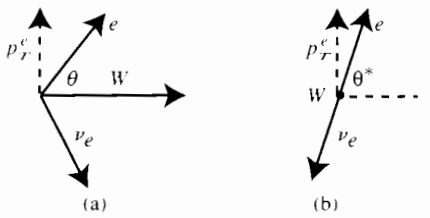


Fig. 9.16. The momenta (a) in the laboratory frame and (b) in the centre of mass frame of the $W$.

momentum is known. However, we can measure $M_W$ with the 'Jacobian peak' method.

Figure 9.16(a) gives a scheme of the $W$ decay kinematic in the laboratory frame. The $W$ momentum component transverse to the beam is very small in general. Neglecting it in a first approximation, the flight direction of the $W$ is the direction of the beams. Consider the electron momentum, which is measured. Its component normal to the $W$ motion, $p_T$ is equal in the laboratory frame and in the centre of mass frame (Fig. 9.16(b))

$$p_T = \frac{M_W}{2} \sin \theta^*. \tag{9.69}$$

Let $dn/d\theta^*$ be the decay angular distribution in the rest frame of the $W$. The transverse momentum distribution is then given by

$$\frac{dn}{dp_T} = \frac{dn}{d\theta^*} \frac{d\theta^*}{dp_T}. \tag{9.70}$$

The quantity $d\theta^*/dp_T$ is called the Jacobian of the variable transformation. Its expression is

$$\frac{dn}{dp_T} = \frac{1}{\sqrt{(M_W/2)^2 - p_T^2}} \frac{dn}{d\theta^*}. \tag{9.71}$$

The essential point is that the Jacobian diverges for

$$p_T = M_W/2. \tag{9.72}$$

Consequently, the $p_T$ distribution has a sharp maximum at $M_W/2$. Notice that the conclusion does not depend on the longitudinal momentum of the $W$, which may be large. The position of the maximum does, on the other hand, depend on the transverse momentum of the $W$, which, as we have said, is small but not completely negligible. Its effect is a certain broadening of the peak.

The electron transverse momentum distribution for the $W$ events is shown in Fig. 9.17, where the Jacobian peak is clearly seen. From this distribution UA1 measured $M_W = 83$ GeV, with $\pm 3$ GeV uncertainty, substantially determined by the systematic uncertainty on the energy calibration. UA2 measured $M_W = 80\,\text{GeV}$ with an uncertainty of $\pm 1.5$ GeV.

A further test of the electroweak theory is the measurement of the electron helicity in the decay $W \to e\nu$. Consider the process in the $W$ rest frame as in Fig. 9.18.

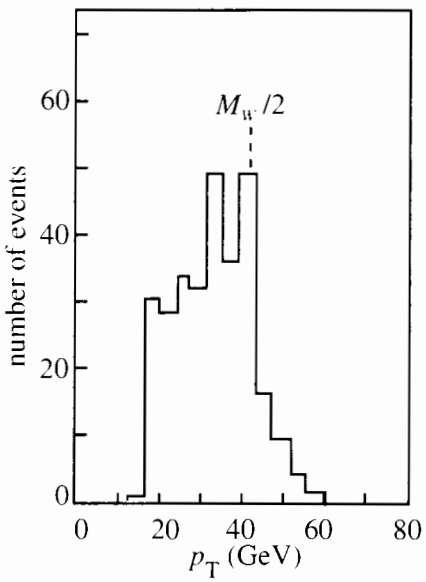


Fig. 9.17. Electron $p_T$ distribution for $W$ events. (Adapted from Albajar *et al.* 1989)

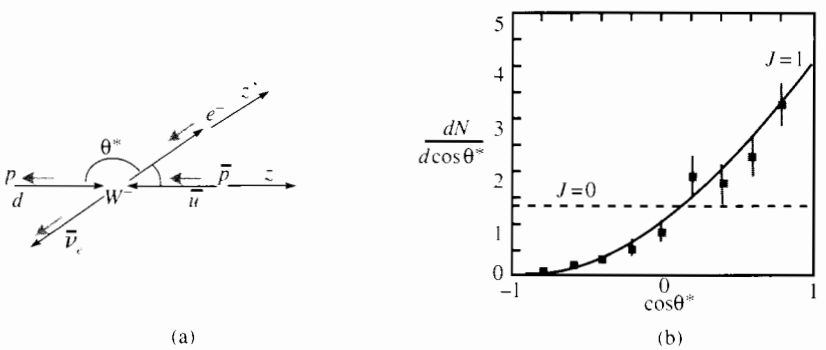


(a) (b)

Fig. 9.18. (a) Kinematics of the $W$ production and decay. (b) Angular distribution measured by UA1. (Adapted from Albajar *et al.* 1989)

For the $V-A$ structure of the CC weak interactions the leptons are left, and, if their energy is much larger than their masses as in the present case, their helicity is $-1$; the antileptons are right, with helicity $+1$. We take $z$, the direction of the beams, as the quantisation axis for the angular momenta in the initial state, as in Fig. 9.18. The total angular momentum is $J=1$. As already seen, since the $W$ production is due to valence quarks, we know that the initial quark has the direction of the proton, the antiquark that of the antiproton. Therefore, the third component of the angular momentum is $J_z=-1$.

We take the electron direction $z'$ as the quantisation axis in the final state. By the same token the third component is $J_{z'}=-1$. Therefore, the angular dependence of the differential cross section is given by

$$\frac{d\sigma}{d\Omega} \propto \left[d^1_{-1,-1}\right]^2 = \left[\frac{1}{2}(1+\cos\theta^*)\right]^2. \tag{9.73}$$

The distribution measured by UA1 is shown in Fig. 9.18(b); the curve is Eq. (9.73), which is in perfect agreement with the data. The dotted line is the prediction for $W$ spin $J=0$. In this way we measure the $W$ spin.

Notice that the observed asymmetry shows that parity is violated but does not prove that the CC structure is $V-A$. The $V+A$ structure predicts the same angular distribution. Only polarisation measurements can distinguish the two cases.

*Question 9.1* Prove the last statement.

We now consider the discovery of the $Z$. Figure 9.19 shows the UA1 tracking view of a typical $Z \to e^- e^+$ event. Again, the confused view becomes clear with

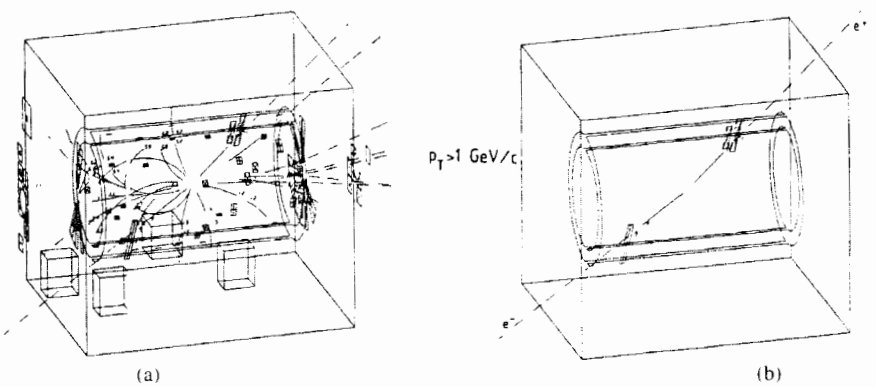


Fig. 9.19. (a) A $Z \to e^- e^+$ event; (b) only tracks with $p_T > 1$ GeV. (Rubbia 1985 © Nobel Foundation 1984)

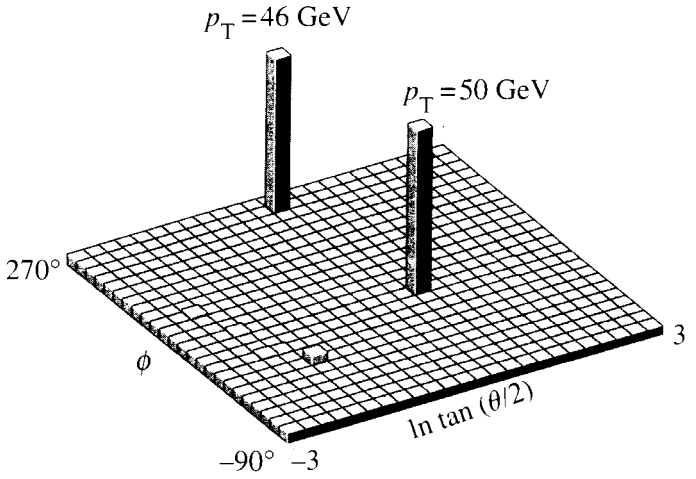


Fig. 9.20. Lego plot of a $Z \rightarrow ee$ event in the UA1 electromagnetic calorimeter.

the selection $p_T > 1$ GeV. Only two tracks remain. One of them is positive, the other negative; for both, the energy as measured in the electronic calorimeter is equal to the momentum measured from curvature.

Figure 9.20 shows the calorimetric view of a $Z \rightarrow e^- e^+$ event: two localised, isolated energy deposits appear in the electromagnetic calorimeter.

The mass of $Z$ is obtained by measuring the energies of both electrons in the electromagnetic calorimeters and the angle between their tracks in the central detector. Figure 9.21 is the $M_Z$ distribution of the first 24 UA1 events. The average is $M_Z = 93$ GeV with a systematic uncertainty of $\pm 3$ GeV; the UA2 measurement gave $M_Z = 91.5$ GeV with a systematic uncertainty of $\pm 1.7$ GeV.

In conclusion, by 1983 the UA1 and UA2 experiments had confirmed that the vector mesons predicted by the electroweak theory exist and have exactly the predicted characteristics.

Particularly important is the ratio of the two masses, experimentally because it is not affected by the energy scale calibration and theoretically because it directly provides the weak angle. Indeed, Eq. (9.28) valid at the tree-level, gives

$$\cos^2 \theta_W = 1 - (M_W/M_Z)^2. \tag{9.74}$$

The ratio of the masses measured by UA1 and UA2 gives

$$\text{UA1}: \sin^2 \theta_W = 0.211 \pm 0.025 \qquad \text{UA2}: \sin^2 \theta_W = 0.232 \pm 0.027. \tag{9.75}$$

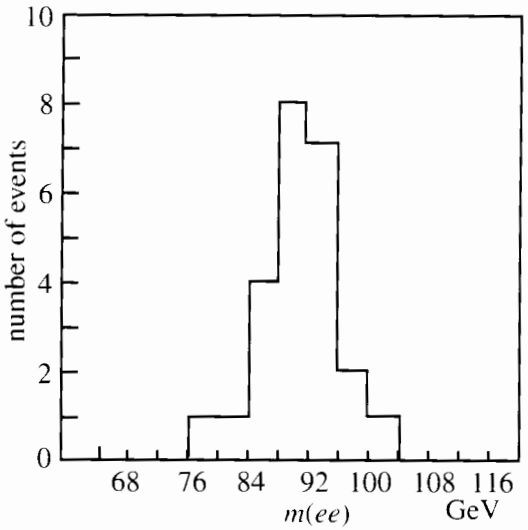


Fig. 9.21. Distribution of $m\,(e^-e^-)$ for the first 24 UA1 events. (Adapted from Albajar *et al.* 1989)

These values are in agreement with the low-energy measurements we mentioned in Section 9.4. We shall come back to this point in Section 9.8 for a more accurate discussion.

*Question 9.2* Does the $Z$ decay into two equal pseudoscalar mesons? And into two scalar mesons?

*Question 9.3* In their first data-taking period, UA1 and UA2 collected $\sim$300 $W$ and $\sim$30 $Z$ each. What is the principal source of uncertainty on the $W$ mass? On the $Z$ mass? On their ratio?

Before closing this section, let us see how the quarks appear in a hadronic collider. As we know, to observe a quark we should not try to break a nucleon in order to extract one of them, rather we must observe the hadronic energy flux in a high-energy collision at high momentum transfer. One of the first observations of UA2 (Banner *et al.* 1982) and UA1 was that of events with two hadronic jets in back-to-back directions. They are violent collisions between two quarks, which in the final state hadronise into jets. More rarely a third jet was observed, due to the radiation of a gluon.

The lego plot of a two-jet event as seen in the UA1 calorimeter is shown in Fig. 9.22. Comparing it with Fig. 9.20 we see that the two quarks, as seen in the calorimeter, are very similar to electrons, with some differences: the peaks are

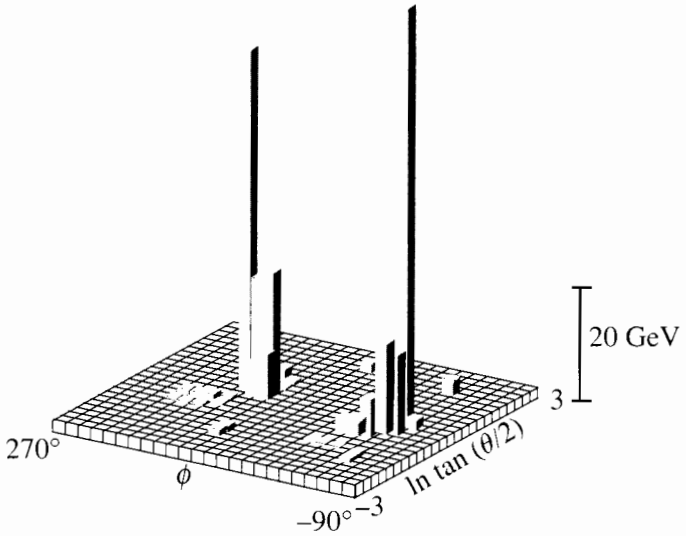


Fig. 9.22. Two quark jets in the UA1 hadronic calorimeter. (Adapted from Albajar *et al.* 1987)

wider and more activity is present outside them, two features that are well understood by thinking of the antiscreening QCD phenomenon.